We are IntechOpen, the world's leading publisher of Open Access books Built by scientists, for scientists

4,800
Open access books available

122,000
International authors and editors

135M
Downloads

Our authors are among the

154
Countries delivered to

TOP 1%
most cited scientists

12.2%
Contributors from top 500 universities

CLARIVATE ANALYTICS BOOK CITATION INDEX INDEXED

WEB OF SCIENCE™

Selection of our books indexed in the Book Citation Index in Web of Science™ Core Collection (BKCI)

Interested in publishing with us?
Contact book.department@intechopen.com

Numbers displayed above are based on latest data collected.
For more information visit www.intechopen.com

5

The Investigation of the Hydrodynamics of an Artificial Reef

Yan Liu[1], Guohai Dong[1], Yunpeng Zhao[1],
Changtao Guan[2,3] and Yucheng Li[1]
[1]*Dalian University of Technology*
[2]*Yellow Sea Fisheries Research Institute*
[3]*Key Laboratory of Fishery Equipment and Engineering*
China

1. Introduction

Marine resources have been declining all over the world in recent decades. The natural reefs of the world are experiencing higher use and pressures, resulting in anthropogenic influences that are deteriorating coral reefs and causing poor water quality. Artificial reefs are manmade structures that are placed on the seabed deliberately to mimic some characteristics of a natural reef. **(Jensen, 1998)**. Both Japan and the United States have been using artificial reefs for at least 200 years. The first artificial reef was deployed in Japan in the 1700s, and the primary goal was to increase fish-catch. Nowadays, artificial reefs in Japan involve diversified types, integrated materials, complicated structures and large-scale design. The first documented artificial reef in the United States dates from 1830, when logs and rocks were sunk off the coast of South Carolina to improve fishing **(Williams, 2006)**. In many countries, artificial reefs have become important elements in the plans for integrated fishery management. Diverse shapes for artificial reefs, such as cube reefs, circular reefs, cross-shaped reefs and so on, provide favorable circumstances for fish perching, foraging, breeding and defense from enemies. Most artificial constructions in the marine environment consist of a variety of non-natural materials. At present, concrete is most commonly employed as a reef material, including cubes, blocks and pipes. Concrete has also been used in combination with other reef materials such as steel, quarry rock, tires and plastic **(Baine, 2001)**. Many of the world's largest artificial reefs have been deployed as part of a national fisheries program in Japan, where large steel and concrete frameworks have been carefully designed to withstand strong ocean currents **(Seaman, 2007)**. Other popular reef building materials include natural stone and rock, the latter constructed from wide-ranging materials including canvas, anchor blocks, and others. The different faunal assemblages associated with artificial reefs are determined by the physical and chemical nature of the reef materials. **Walker, et al (2002)** quantitatively compared the fish abundance, fish species richness and fish biomass on artificial reef modules constructed of various materials.

There are several proposed mechanisms to explain how artificial reefs increase total biomass production. First, an artificial reef can provide additional food and increase feeding efficiency, and many studies have reported observations of fishes feeding at artificial reefs.

Secondly, affording shelter from predation implies higher survival at artificial reefs than in natural habitats, which is supported by some early experimental studies. **Hixon & Beets, (1989)** tested two corollaries of the limited shelter hypothesis by conducting the experiments in Perseverance Bay, St. Thomas, U.S. Virgin Islands. They suggested that artificial reefs designed for persistent fisheries should include both small holes for small fishes (as refuges from predation) and large holes for predatory species (as home sites). **Leitao, et al (2008)** studied the effect of predation on artificial reef juvenile demersal fish species. The results indicated that interspecific interactions (predator–prey) are important for conservation and management and for the evaluation of the long-term effects of reef deployment. Third, artificial reefs increase the production of natural reef environments by creating vacated space. **Einbinder, et al. (2006)** experimentally tested whether artificial reefs change grazing patterns in their surrounding environment. The results suggest that herbivorous fishes are attracted to the artificial reefs, creating a zone of increased grazing. It is necessary to consider their overall influence on their natural surroundings when planning deployment of artificial reefs. Fourth, artificial reefs have been demonstrated a potential tool for the restoration of marine habitats. The proper role of artificial habitats in aquatic systems continues to be a topic of debate among ecological engineers. A detailed description of the role of artificial reef habitats in the restoration of degraded marine systems has been given by **Seaman, (2007)**. Finally, an important aspect of artificial reefs includes the flow pattern effect. Recent studies have demonstrated the value of investigating the flow field effect in and around artificial reefs as a means of identifying their ecological effect on the proliferation of fishery resources **(Lin & Zhang, 2006)**. When an artificial reef is deployed at the bottom of the sea, many kinds of flow patterns characterized by intense velocity gradients, flow turbulence, vortices, and so on are aroused and develop depending on the shapes, sizes and the different arrangements of artificial reefs. **Zhang & Sun, (2001)** discovered that considerable local upwelling current fields and eddy current fields are generated at the front and the back of artificial reefs, respectively. Upwelling enhances biological productivity, which feeds fisheries, and it is richer in nutrients. Meanwhile, a geometric shaded area is distributed within and around the reef. Consequently, algae and plankton thrive, and therefore, the reefs not only provide a shelter from predators but also an abundant food source.

In view of the above, flow field research is key to the research of artificial reef eco-efficiency. **Liu, et al. (2009)** simulated the flow fields around solid artificial reefs models with different shapes, including cubes, pyramids and triangular prisms, by mean of wind tunnel experiments and numerical simulation methods. **Su, et al. (2007)** conducted particle image velocimetry (PIV) measurements to study the flow patterns within and around an artificial reef. The PIV results were then used to verify the numerical results obtained from finite volume method (FVM) simulations. In engineering practice, the stability of artificial reefs is an important issue in preventing the failure of reef units due to current action. The stability of reefs and sediment erosion on the bottom of artificial reefs rely on the interactions among the current-bottom material-reef system. In this study, the flow field patterns around a hollow cube artificial reef were investigated by employing FVM simulation with unstructured tetrahedral grids for solution of three-dimensional incompressible Reynolds-averaged Navier-Stokes equations. A renormalization group (RNG) k-ε turbulence model was embedded in the Navier-Stokes solver. The pressure and velocity coupling was solved with the SIMPLEC algorithm at each time step. To validate simulation predictions, non-

invasive PIV measurements were conducted to measure the flow patterns around the artificial reef. On the basis of the numerical model validation, the flow fields of hollow cube artificial reefs with different altitudes were analyzed using the numerical model. The effects of spacing on the flow field around the parallel and vertical two hollow cube artificial reefs were also analyzed in detail.

2. Numerical methods

Computational fluid dynamics (CFD) are generally used by engineers to solve fluid dynamics problems that involve solving some form of the Navier-Stokes equations. The numerical simulation analysis of flow fields around artificial reef is based on a dynamic, full 3D model elaborated with the aid of FLUENT 6.3 commercial code. The finite volume method are used in the study to solve the three-dimensional Reynolds-averaged Navier-Stokes (RANS) equations for incompressible flows.

2.1 Hypotheses

1. Incompressible, viscous, Newtonian fluid for the water.
2. Isothermal flows, regardless of heat exchange in the water.
3. Flow is in the non-steady state.
4. The water surface is modeled as a "moving wall" with zero shear force and the same speed as the incoming fluid.

2.2 Hydrodynamic equations solved

The equations solved are the momentum equation, also known as the Navier-Stokes equation, and the continuity equation. This approach is useful for solving laminar flows, but, for turbulent flows, the direct solving of all the vortices in a turbulent flow is expensive. Therefore, a model for turbulence must be added. There are several types of turbulence models available. The most common are the RANS models and large eddy simulation models. In the present study, the two-equation RANS models were chosen to resolve the ensemble averaged flow and model the effect of the turbulent eddies. In the RANS equations, various instantaneous physical parameters are replaced by the time-averaged value. Incompressible flow is assumed such that the equations are as follows:

Momentum equation

$$\rho \frac{\partial}{\partial x_j}(u_i u_j) = -\frac{\partial P}{\partial x_i} + \frac{\partial}{\partial x_j}(\mu \frac{\partial u_i}{\partial x_j} - \rho \overline{u_i' u_j'}) + S_i \tag{1}$$

Continuity equation

$$\frac{\partial u}{\partial x} + \frac{\partial v}{\partial y} + \frac{\partial w}{\partial z} = 0 \tag{2}$$

For Eq. (1), ρ is the mass density; u_i is the average velocity component for x, y, z; P is a body of fluid pressure on the micro-volume; μ is the viscosity; u' is the fluctuation velocity; and i, j=1, 2, 3 (x, y, z). S_i is the source item.

In eddy viscosity turbulence models, the Reynolds stresses are linked to the velocity gradients via the turbulent viscosity, and this relation is called the Boussinesq assumption, where the Reynolds stress tensor in the time averaged Navier-Stokes equation is replaced by the turbulent viscosity multiplied by the velocity gradients. The two-equation models assume an eddy-viscosity relationship for the Reynolds stresses in Eq. (1) given by

$$-\rho\overline{u_i' u_j'} = \mu_t\left(\frac{\partial u_i}{\partial x_j} + \frac{\partial u_j}{\partial x_i}\right) - \frac{2}{3}\rho k\delta_{ij} \tag{3}$$

where μ_t is the eddy viscosity and δ_{ij} is the Kronecker delta.

The k–ε two equations model has become the workhorse for practical engineering modeling of turbulent flows due to its robustness, economy and reasonable accuracy for a wide range of flows. In the derivation of the k–ε model, it is assumed that the flow is fully turbulent and that the effects of molecular viscosity are negligible. Therefore, the model is only valid for fully turbulent flows. An improved version of the k–ε turbulence model, the renormalization group (RNG) k–ε model, is adopted here, which is derived from the transient Navier-Stokes equation and employs a new mathematical method called a "renormalization group". RNG k–ε model provides an option to account for the effects of swirl or rotation by modifying the turbulent viscosity appropriately

The new turbulent equations for "k" and "ε" are introduced as follows.

k equation

$$\frac{\partial}{\partial t}(\rho k) + \frac{\partial}{\partial x_i}(\rho k\overline{u_i}) = \frac{\partial}{\partial x_j}\left(\alpha_k \mu_{eff}\frac{\partial k}{\partial x_j}\right) + G_k - \rho\varepsilon \tag{4}$$

ε equation

$$\frac{\partial}{\partial t}(\rho\varepsilon) + \frac{\partial}{\partial x_i}(\rho\varepsilon\overline{u_i}) = \frac{\partial}{\partial x_j}\left(\alpha_\varepsilon \mu_{eff}\frac{\partial \varepsilon}{\partial x_j}\right) + C_{1\varepsilon}\frac{\varepsilon}{k}G_k - C_{2\varepsilon}\rho\frac{\varepsilon^2}{k} - R_\varepsilon \tag{5}$$

In Eqs. (4-5), a_k and a_ε are the inverse effective Brandt numbers for the k and ε equations, respectively; G_k is expressed by the mean flow velocity gradient arising from the turbulent kinetic energy; $C_{1\varepsilon}$ and $C_{2\varepsilon}$ are constants with values of 1.42 and 1.68, respectively; and μ_{eff} is the validity viscosity coefficient defined as follows:

$$\mu_{eff} = \mu_t = \rho C_\mu \frac{k^2}{\varepsilon} \tag{6}$$

C_μ is a constant equal to 0.0845.

The additional term R_ε is the major difference between the RNG k-ε model and the standard k-ε, which significantly improves the accuracy for a high strain rate and large degree of crook flows. This term is given as

$$R_\varepsilon = \frac{C_\mu \rho \eta^3 (1 - \eta/\eta_0)}{1 + \beta\eta^3}\frac{\varepsilon^2}{k} \tag{7}$$

Here, $\eta=Sk/\varepsilon$ and η_0 and β are constants equal to 4.380 and 0.012, respectively.

2.3 Boundary conditions

The boundaries of the computational domain are categorized as inlet, outlet, and wall. The mean velocity is specified at the inlet where the turbulent kinetic energy and specific dissipation rate are calculated according to the computational formulas of the turbulence parameter. The flow at the outlet is not defined and is allowed to change as the hydrodynamic pressure at all the boundaries is calculated from inside the domain. A stationary no-slip boundary condition is prescribed on the flume and artificial reef, and the undisturbed free surface is treated as a "moving wall", which has zero shear force and the same speed as the incoming fluid. For coarse meshes, boundary layers cannot be discretized in sufficient detail. The standard wall functions based on the proposal of Launder and Spalding was used to bridge the solution variables in the cell next to the wall to the values at the wall.

2.4 Meshing

The computational grids are shown in Fig. 1. Meshes for modeling flow fields of artificial reefs using FLUENT were created in GAMBIT. In this work, all grids used were unstructured, and the TGrid meshing scheme was used to generate unstructured tetrahedral grids. Grids around the artificial reef were generated densely, and other domains were generated sparsely to reduce unnecessary calculations.

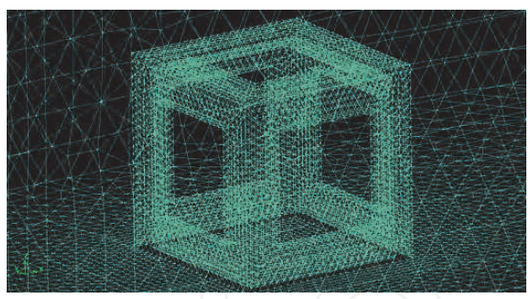

Fig. 1. Computational grids

2.5 Finite volume discretization

The equations were solved using a FVM, where the equations were integrated over a control volume. The control volume integrals were discretized into sums, which yielded discrete equations. The discrete equations were applied to each control volume. The values of the variables in the equations were solved by upwind discretization schemes. The basic concept of upwind schemes is that the face value of a given variable is defined from the cell center value in the cell upstream of the face. Upstream is defined relative to the fluid velocity normal to the face. The second-order upwind schemes were employed for the turbulent kinetic energy and turbulent energy dissipation rate here. In FLUENT6.3, all computational work was performed with the 3D pressure-based solver in a first-order implicit unsteady formulation. Gradients were estimated by the Green-Gauss cell-based method. The

SIMPLEC algorithm was employed for pressure-velocity coupling. High-resolution discretization schemes were used for the discretization of mass and momentum equations. The equations were linearized using an implicit solution and iterated to achieve a converged solution. Convergence was assumed for each time step when all residuals fall below 10^{-3}, and a maximum of 100 iterations per time step was considered if the residuals failed to pass these thresholds.

3. Experimental methods

In recent decades, PIV has become a powerful technique for measuring instantaneous velocity fields. Highly reflective particles are thrown into the flume, and a light sheet produced by a laser is projected into the flow field of interest. Then, the light reflected by these particles is captured by a high-speed camera. The calculation of the speed of the particles in the raw particle images is based on the cross-correlation, and techniques such as the erroneous vector correction are also employed to reduce the computing error. The PIV systems are described in detail below.

The structure and arrangement of a single hollow cube artificial reef model are shown in Fig. 2. In this study, the reef block model was scaled by a factor of 1:20 to satisfy the physical constraints of the flume measuring area and avoid inducing an undesirable channel wall effect. The hollow cube artificial reef model was composed of five Plexiglas faces, with a width of 7.5 cm and 4.5 cm square openings. The artificial reef model was arranged at 90^0 and 45^0 angles at the bottom of the flume. All of the test sections are based on the axial plane of the artificial reefs.

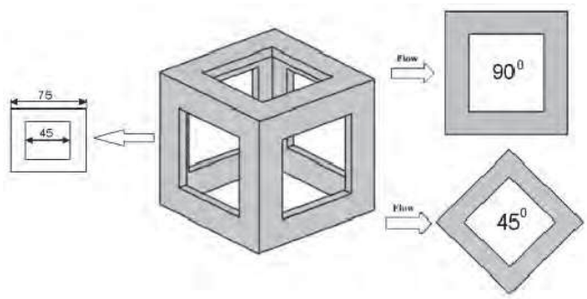

Fig. 2. Structure and arrangements of a single hollow cube artificial reef model

As shown in Fig. 3, a three-dimensional coordinate system (x-y-z) was set up to build the PIV experiment with the origin at the center of the artificial reef. The internal dimensions of the flume were 22.00×0.45×0.60 m (length ×width ×height), and the water depth of test (H) was 0.4 m. The maximum test section was 45 cm wide, 60 cm deep and 100 cm long. The sides and bottom of the test area in the center of the water channel were composed of glass to facilitate PIV measurement of the flow fields at various positions around the artificial reef model. A centrifugal pump was fixed on the left of the flume and affords flow velocities of U_1=6.7, U_2=11.0 and U_3=18.0 cm/s. The experimental flow velocities were chosen according to the characteristic flow rate of the practical sea area, and the corresponding physical values were 0.3 m/s, 0.5 m/s and 0.8 m/s. The inlet flow velocity was measured using acoustic Doppler current velocimetry.

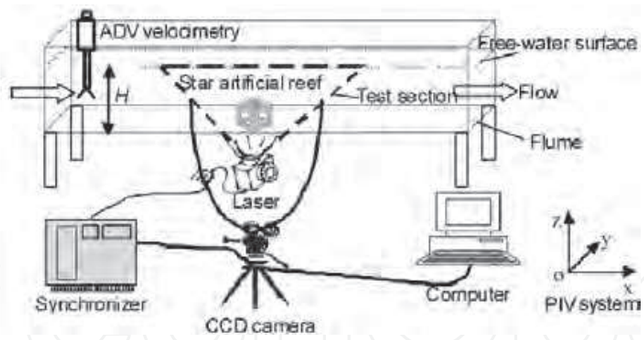

Fig. 3. Schematic diagram of the experimental apparatus and the PIV system

The basic optical devices of the PIV system were designed according to the experimental configuration specified by TSI Inc (USA). The light sheets were generated by an Nd: YAG laser capable of producing 3-5 ns, 120 mJ pulses at a repetition frequency of 15 Hz. The digital images were captured using a high-resolution CCD camera with two million pixels. The maximum frame rate of the camera was 32 f/s. A CCD camera (Power View 4MP) coupled to PC image acquisition software was used to acquire images. The operation of the laser and the camera was synchronized by a digital delay pulse generator. Selecting reflective polyvinyl chloride powder with a mean diameter of 10 μm and density of 1050 kg/m^3 was added to the water as a trace particle.

4. Flow field characteristics of a single hollow cube artificial reef

It is known that the structure of flow field within and around artificial reefs plays an important role in their ecological effects. The flow field effect is one of the most important ecological effects, therefore making artificial reefs with configurations specifically designed to induce suitable flow field structures has been of great interest to marine ecologists and engineers in recent decades. The upwelling and back vortex flow is the major flow field character, which is an important hydrodynamic characteristic of artificial reefs. Some nomenclatures are listed for analyzing and discussing these flow field characteristics qualitatively and quantitatively. The upwelling field is defined where the flow velocity of

Nomenclature	
U_{in}: inlet current velocity (cm/s)	h: the height of artificial reef model (cm)
H: the depth of water (cm)	r: the ratio of reef height to water-depth
H_{up}: the height of upwelling field (cm)	S_{up}: the area of upwelling field (cm^2)
S_e: the area of back vortex flow (cm^2)	L_e: the length of back vortex flow (cm)
V_{max}: the maximum upwelling current velocity (cm/s)	V_a: the average upwelling current velocity (cm/s)
S: the incident flow area of artificial reef model (cm^2)	S_{upA}: unit reef effect for the area of upwelling
S_{eA}: unit reef effect for the area of back vortex flow field	H_{upA}: unit reef effect for the height of upwelling field
L_{eA}: unit reef effect for the length of back vortex flow field	L_{rp}: the length of water current reattachment point from the end of reef model (cm)

the axis z (height) orientation is equal to or greater than ten percent of inlet flow velocity. A clockwise rotation vortex is generated at the rear of the artificial reef and is called the back vortex flow field. Compared with the inlet flow velocity, the flow velocity in the back vortex flow field is slower. Therefore, the back vortex flow field is also called the slow flow region. The water current reattachment point is an important characteristic quantity and is located downstream of the artificial reef where the flow velocity is on the verge of zero. All of the arguments for the upwelling current and back vortex flow are on the vertical two-dimensional central plane.

4.1 Flow field of a single hollow cube artificial reef

4.1.1 A single hollow cube artificial reef at a 90 degree angle

Figs. 4(a) and 4(b) show the experimental and numerical results for the flow field velocity vector diagram of a single hollow cube artificial reef with a 90 degree angle, respectively. In front of the artificial reef, the flow velocities slow down due to the reef resistance causes. Several narrow regions with different values of flow velocities spread in the upstream field, and the flow velocities increase gradually with height. Within the reef, the upper and bottom regions of the flow field have a low velocity, while the regions in the opening have a high velocity, which is approximately the incoming flow velocity. The reason is that the flow into the reef is obstructed by the two vertical members on both sides of the cube side face but can enter freely through the opening located in the center of the face. Figs. 4(a) and 4(b) also show that a low velocity flow field is formed in the area downstream of the reef. Experimental and simulation results show a similar velocity distribution around the artificial reef. The overall velocity vector diagrams of the two figures are in good agreement.

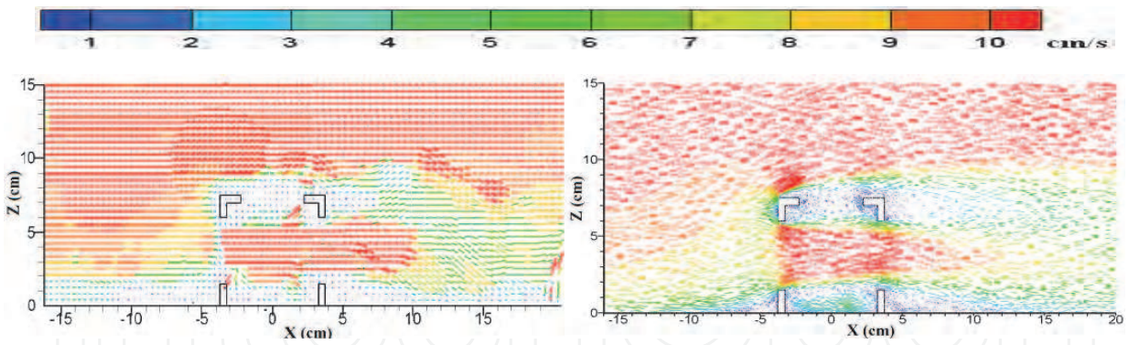

(a) Experimental results (b) Simulation results

Fig. 4. Flow field velocity vector diagram of a hollow cube artificial reef with a 90 degree angle

Fig. 5 compares the scale and intensity of upwelling and back vortex flow field between the experimental and simulation results at a 90 degree angle. The height (H_{up}) and the area (S_{up}) of upwelling field by simulation are close to the experimental data. The computational average upwelling current velocities (V_a) are slightly higher than the experimental results. A major gap exists in the length of the back vortex flow (L_e), especially with a lower inlet flow velocity. In the field of the back vortex flow, the flow velocity is very slow and is on the verge of zero at the water current reattachment point, such that the performance of the

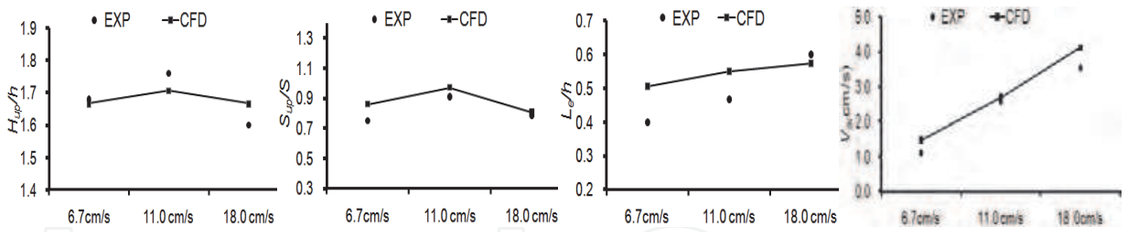

Fig. 5. H_{up}/h, S_{up}/S, L_e/h and V_a of experimental and simulation results at a 90 degree angle

tracing particles is weakened and causes a larger error. The mean error of upwelling and back vortex flow between the experiment and simulation is lower than 11%, and both of the results have an identical variation trend with the increase of the incoming flow velocity.

4.1.2 A single hollow cube artificial reef at a 45 degree angle

Figs. 6(a) and 6(b) present the experimental and numerical results obtained for the velocity vector diagrams of a hollow cube artificial reef with 45° angle. The flow structures observed at this angle are not the same as those for a 90° angle, especially inside the artificial reef. At this angle, the water flow is obstructed by the side face of the artificial reef, and no fluid can directly enter the reef in the middle. In the upstream, the slow flow velocity field is mainly distributed at the bottom or close to the reef side face. The flow velocity, both in the experiment and simulation, in most regions within the reef, is less than 2.0 cm/s, and the maximum velocity is only half of the inlet flow velocity. There is a large difference for the flow field structure in the rear of the artificial reef between the two arrangements. A large and complicated vortex is formed immediately downstream of the reef. The low flow velocity conditions in this region indicate the presence of a desirable shading effect, i.e., fish can rest and seek shelter in this suitable environment. For Fig. 6 (a) and (b), the numerical simulation predicts a flow field that is comparatively similar with the experimental results.

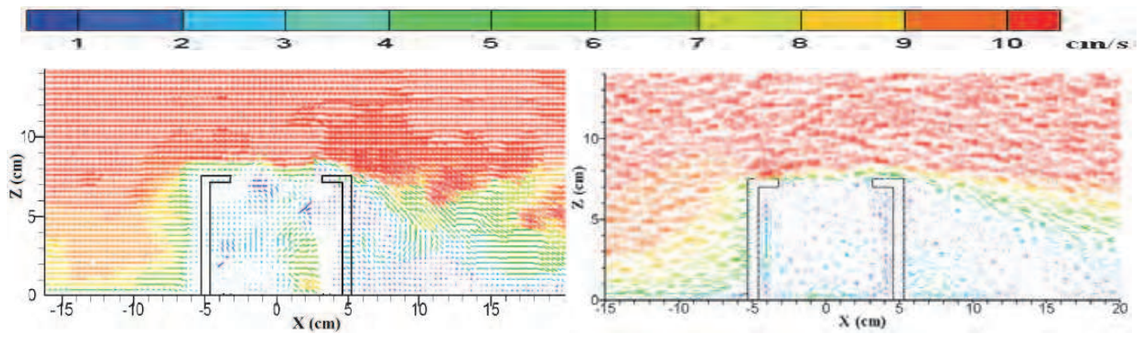

(a) Experimental results (b) Simulation results

Fig. 6. Flow field velocity vector diagram of a hollow cube artificial reef with a 45 degree angle

Fig. 7 shows the comparisons of the scale and intensity of the upwelling and back vortex flow field that are derived from the experiment and numerical simulation at a 45 degree angle. A good agreement was found between the two results. Nonetheless, there is a large

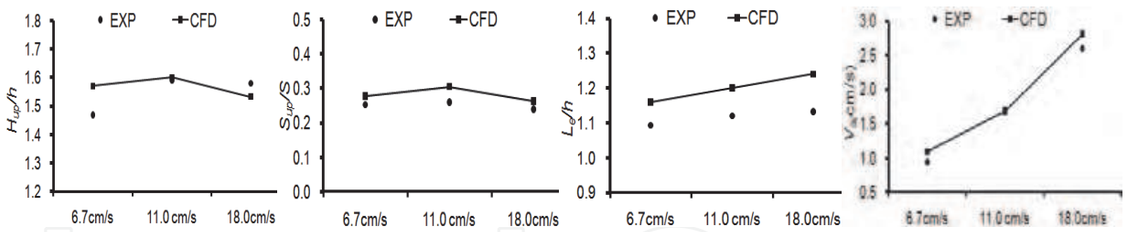

Fig. 7. H_{up}/h, S_{up}/S, L_e/h and V_a of experimental and simulation results at a 45 degree angle

difference in the comparison of the height of upwelling field when the inlet flow velocity is 6.7 cm/s, which may be caused by the lack of particle concentration in the experiment. The mean error between the experiment and simulation was within 8%. In this arrangement, the resistance to the water flow is intensified, and a large pressure gradient is generated around the reef so that a large-scale back vortex flow is produced.

4.1.3 Brief conclusion

In this small chapter, the flow field around a single hollow cube artificial reef is analyzed qualitatively and quantitatively by physical experiment and numerical simulation. The flow field within and in back of the artificial reef with a 45 degree angle has a lower flow velocity than a 90 degree angle. The scale and intensity of the upwelling field of artificial reef with a 90 degree angle are larger than a 45 degree angle. However, a biggish area of slow flow field is obtained at a 45 degree angle. The results of numerical simulation show good agreements with experimental measurements which provide powerful support for the next numerical analysis with regard to the effect of reef height on the flow field of a single artificial reef and the effect of spacing on the parallel and vertical binary combined artificial reefs.

4.2 Effect of reef height on the upwelling field and back vortex flow field

4.2.1 Distributions of the upwelling field

Fig. 8 shows that, with the same inlet velocity, the variation of reef height have nearly no effect on the general structure of the upwelling field. The upwelling field is mainly distributed at the top left corner of the artificial reef and has a fan shaped. The values of the upwelling flow velocity gradually decrease from inside to outside. Generally speaking, the height, breadth and area of the upwelling field always increase with the height of the artificial reef, and these rules are the same as those of a solid cube artificial reef (Pan et al., 2005).

4.2.2 The effect of the reef height on the intensity of the upwelling field

The effect of the reef height on the intensity of the upwelling field was measured by using V_{max} and V_a. The normalized maximum and average upwelling flow velocities are defined as the ratio of the flow velocity to the inlet current velocity, i.e., V_{max}/U_{in} and V_a/U_{in}.

According to Fig. 9, the normalized maximum upwelling flow velocity first increases and then decreases with increasing reef height and peaks at 8.0~9.0, where the value of V_{max} is close to inlet flow velocity. The maximum upwelling flow velocity remains stable when the reef height is less than 7.0; afterwards, it increases rapidly until 9.0. The normalized average

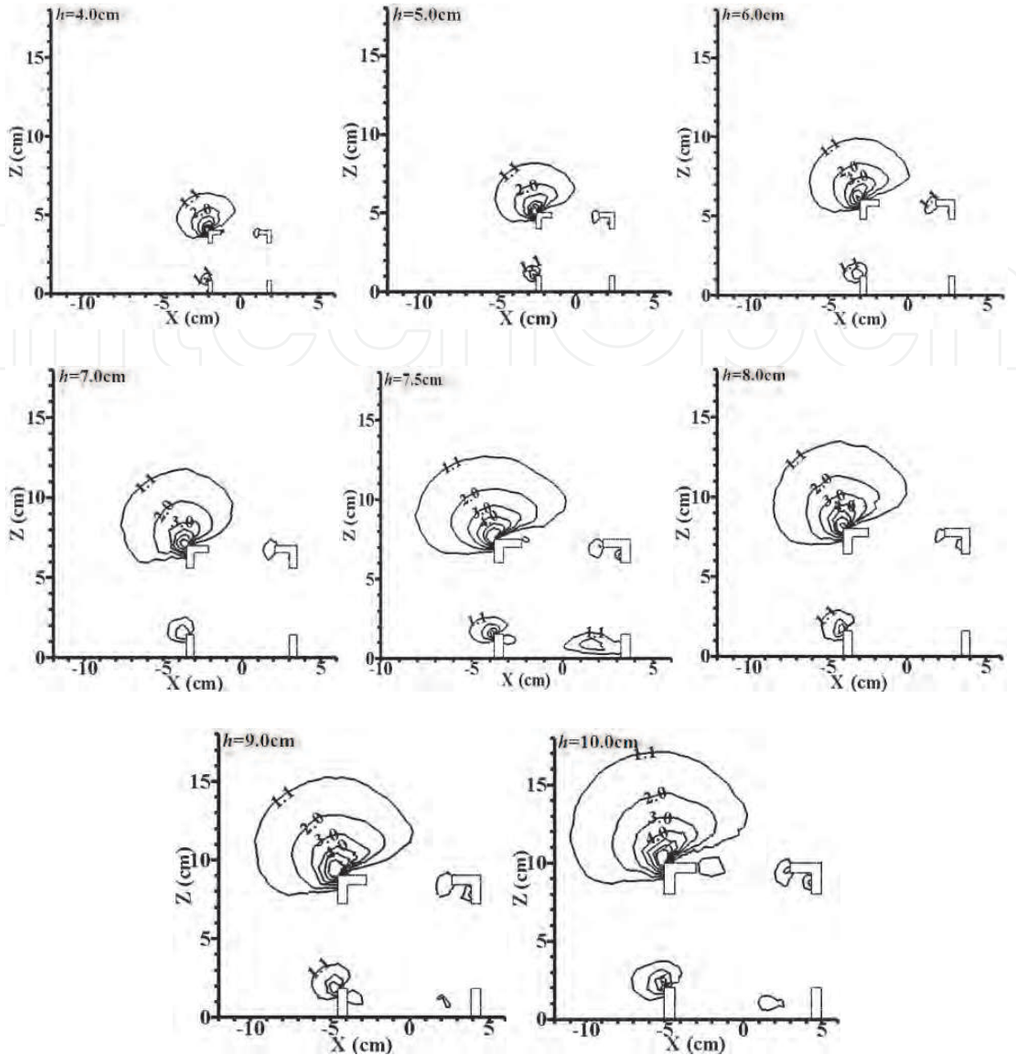

(Inlet velocity is 11.0 cm/s)

Fig. 8. Distribution of the upwelling field with different heights of hollow cube artificial reefs

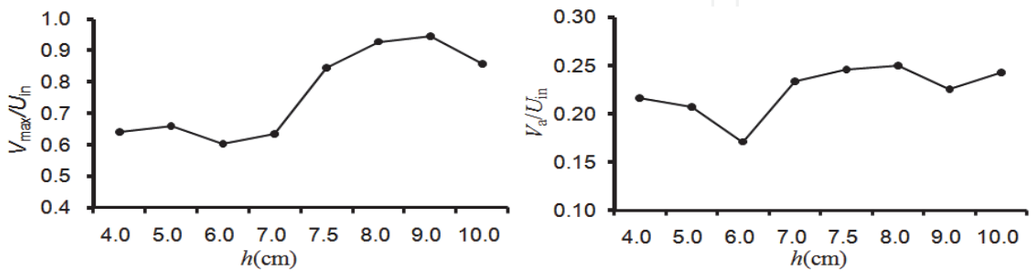

Fig. 9. Normalized maximum and average upwelling velocities with different heights of artificial reefs

upwelling flow velocity does not always increase with the reef height, and the maximum value is obtained at 8.0. The maximum average upwelling flow velocity is nearly a quarter of the inlet flow velocity.

4.2.3 The effect of reef height on the scale of the upwelling field

To find the best size of the artificial reef, a new conception unit artificial reef effect is introduced. It is weighed by length and area, and the unit artificial reef effect relative to the height and area of the upwelling field is represented by $H_{upA}=H_{up}/h$ and $S_{upA}=S_{up}/S$.

As shown in Fig. 10, the result of regression found that the height of the upwelling field and the reef height have a positive linear relationship. The best fit equation between H_{up} (axis y) and h (axis x) is y=1.76x-0.62, which is obtained by the linear regression analysis method, and the R^2 (correlation coefficient) is 0.9997. According to Fig. 10, when the reef height is 7.5 cm and 10.0 cm, H_{upA} (the ration of H_{up} to h) is large. Thus, the preferable unit artificial reef effect relative to H_{up} was acquired at the reef height of 7.5 cm and 10.0 cm.

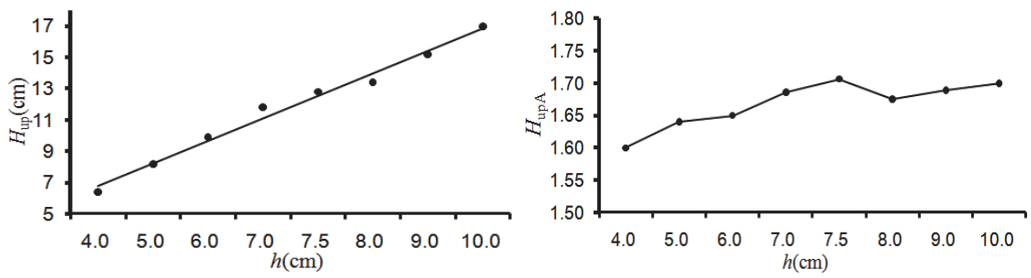

Fig. 10. H_{up} and H_{upA} with different heights of artificial reefs

The area of the upwelling field and the reef height were fitted by the nonlinear regression analysis method, i.e., a second-order polynomial regression. The relationship between S_{up} (y) and h (x) can be expressed by the equation $y=0.86x^2-2.51x+3.87$ and $R^2 = 0.9979$. Fig. 11 shows that the curves of S_{upA} are the same as those for H_{upA}, and both of them acquire a large value at the reef heights of 7.5 cm and 10.0 cm. Thus, a preferable unit artificial reef effect relative to S_{up} is acquired at the reef heights of 7.5 cm and 10.0 cm.

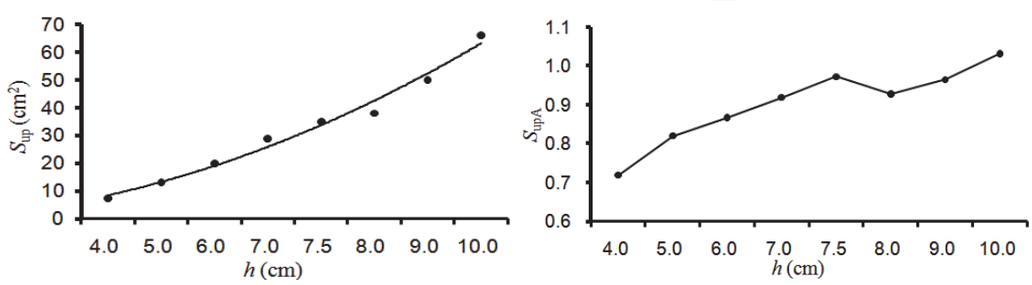

Fig. 11. S_{up} and S_{upA} with different heights of artificial reefs

4.2.4 The effect of reef height on the back vortex flow field

The length of the back vortex flow is almost equal to the distance of the water flow reattachment point from the original point, which is a significant characteristic quantity for back vortex flow. Consequently, L_{rp} and S_e are used to measure the scale of the back vortex flow field. The unit artificial reef effect relative to the length and area of the back vortex flow field is represented by L_{eA} and S_{eA}.

In Fig. 12, the length from the water current reattachment point to the artificial reef and the area of back vortex flow increase continually with increasing reef height. L_{rp} with h (in x axis) presents an exponential growth relationship, and the relevant relational equation is $y=1.09e^{x/5.46}+0.20$. A good correlation coefficient of 0.9976 is acquired. The quadratic polynomial fitted equation for the area of the back vortex flow (y) and reef height (x) is expressed by $y=0.21x^2-1.11x+3.03$, and the homologous correlation coefficient is 0.9973.

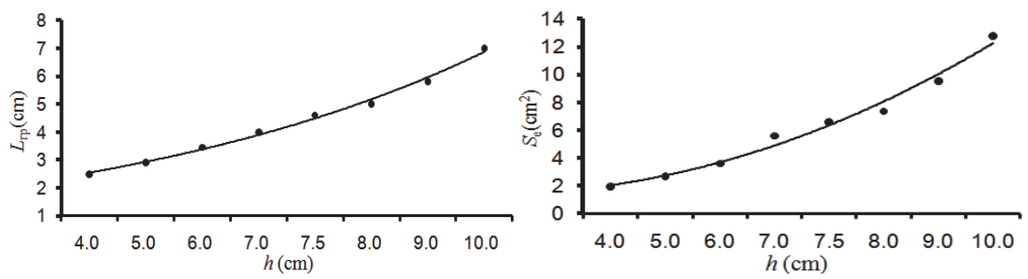

Fig. 12. L_{rp} and S_e with different heights of artificial reefs

As shown in Fig. 13, the variation curves of L_{eA} and S_{eA} with reef height are similar to some degree. The values of L_{eA} and S_{eA} are the minimum at the reef height of 6.0 cm; after that point, there is a relatively fast increase, and a steady value is maintained until 9.0. There are three large values appearing at the heights of 4.0, 7.5 and 10.0, which can be used for the artificial reef designers as a reference.

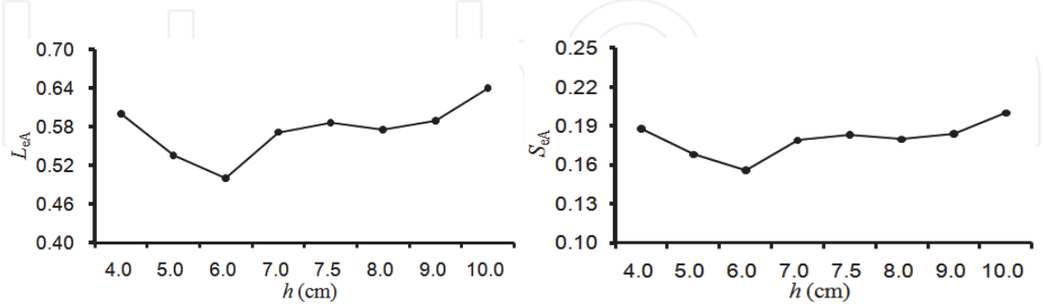

Fig. 13. L_{eA} and S_{eA} with different heights of artificial reefs

4.2.5 Brief conclusion

Considering the economical problems and the stability of artificial reef in a certain depth of water, the height of artificial reef cannot be raised excessively. According to the results

calculated in the numerical simulation, when the reef height is 7.5cm, the efficiency of the reef unit performs best.

4.3 Flow field velocity vector diagram in the horizontal cross-section

The velocity vector diagrams in the horizontal cross-section that is located at the height of 1/2*h* are listed in Fig. 14. Similar structures of the flow field are obtained with different heights of artificial reefs. Within the reef, the flow velocity is close to the inlet velocity. In the area on either side of the artificial reef, the horizontal flow velocity is larger than the inlet flow velocity, and the maximum values are 11.5, 11.9, 11.9, 12.3, 12.9 and 12.9 cm/s, respectively, with increasing reef height. It is apparent that a higher artificial reef will have a wider area in which the horizontal flow velocity is greater than the inlet velocity. The slow flow field is distributed in the front and the back of the reef, where the structures of flow fields vary with the reef height.

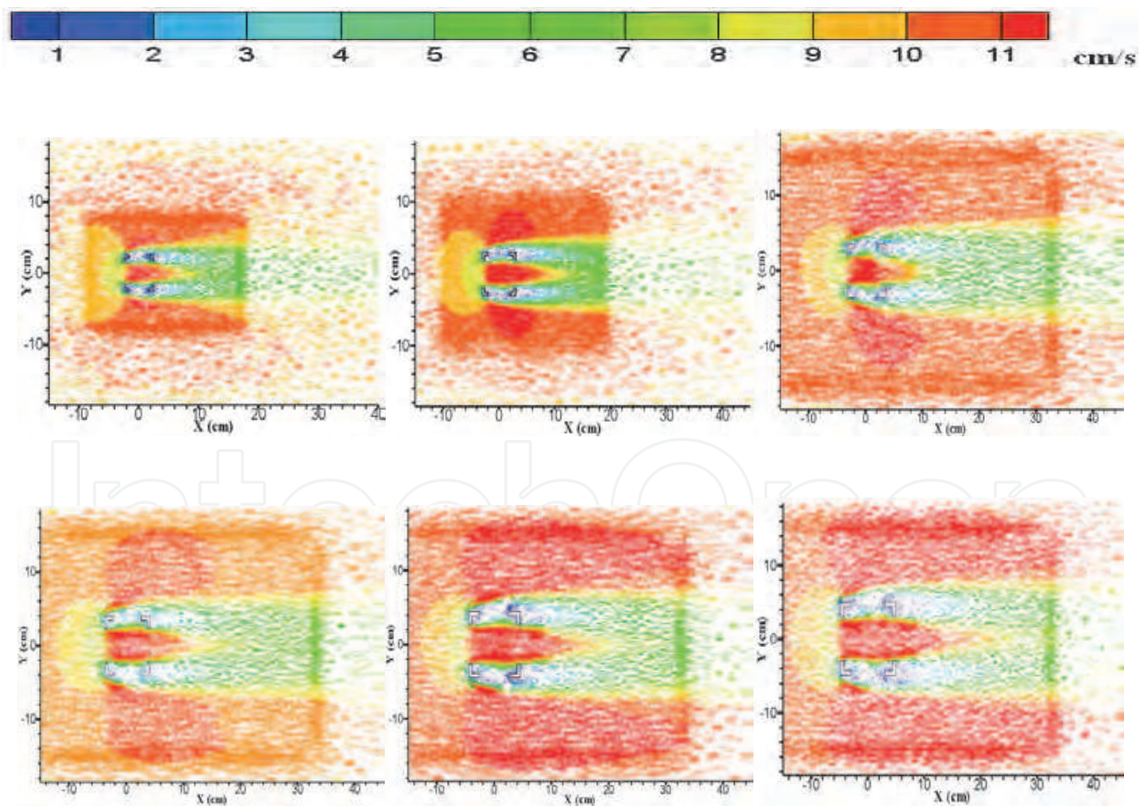

Fig. 14. Velocity vector diagrams in horizontal cross-section with different heights of artificial reefs (the inlet velocity is 11.0 cm/s)

The horizontal flow velocities along the line of y=0 at the horizontal cross-sections of z=1/2*h* are shown in Fig. 15. Similar distributions of flow velocities are found within and around artificial reefs at different heights. In front of the artificial reef, the horizontal flow velocities are approximate and decrease gradually when approaching the artificial reefs. Within artificial reefs, the flow velocities are larger than the inlet flow and peak at the center of the reefs. In addition, with the increase of the reef height, the maximum horizontal flow velocity within the reef is also on the increase. At the rear part of the artificial reefs, the flow velocities show a long-distance attenuation until the locations are sufficiently far away from

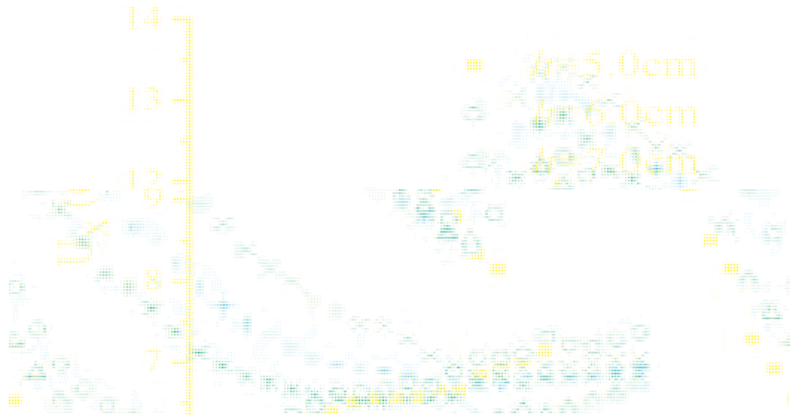

Fig. 15. Distribution of the horizontal flow velocities along the line of Y=0 at the horizontal cross-section of Z=1/2*h* (*h*=5.0, 6.0, 7.0, 8.0, 9.0, 10.0 cm)

the reefs, which are the slow flow regions as mentioned earlier. The smaller the artificial reef is, the lower the horizontal flow velocity is at the rear of artificial reefs. However, there is a special phenomenon where the lowest velocity occurs when the reef height is 7.0 cm. In other words, a preferable slow flow effect is acquired at the reef height of 7.0 cm.

5. Flow field characteristics of two hollow cube artificial reefs

The arrangements of two models of artificial reef are shown in Fig. 16. The spacing of two parallel combined models is 0.5*h*, 1.0*h*, 2.0*h* and 3.0*h*. The spacing of two vertical combined models is 1.0*h*, 2.0*h*, 4.0*h*, 6.0*h*, 8.0*h*, 10.0*h* and 12.0*h* (*h*=7.5 cm).

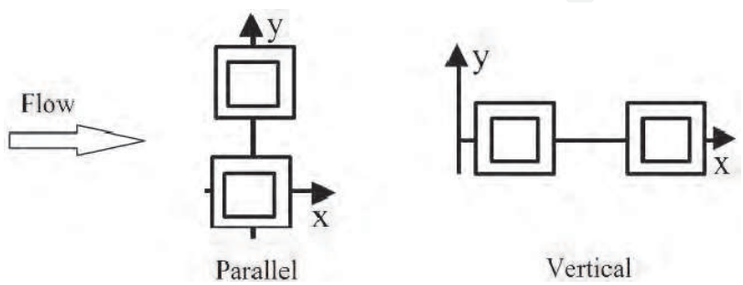

Fig. 16. The arrangements of two hollow cube artificial reefs

5.1 Two parallel hollow cube artificial reefs

Fig. 17 presents the numerical results for the upwelling field of single and two parallel artificial reefs with different spacings. Compared to a single artificial reef, the heights of the upwelling field increase with spacing at first and then decrease until steady. When the spacing is 0.5*h*, the height of the upwelling field reaches the maximum value of 13.8 cm, and the corresponding area is 49.0 cm^2. When the spacing is equal to or larger than 2.0*h*, the height of upwelling field has a steady value of 12.5 cm, and the steady value of the area is 35.0 cm^2.

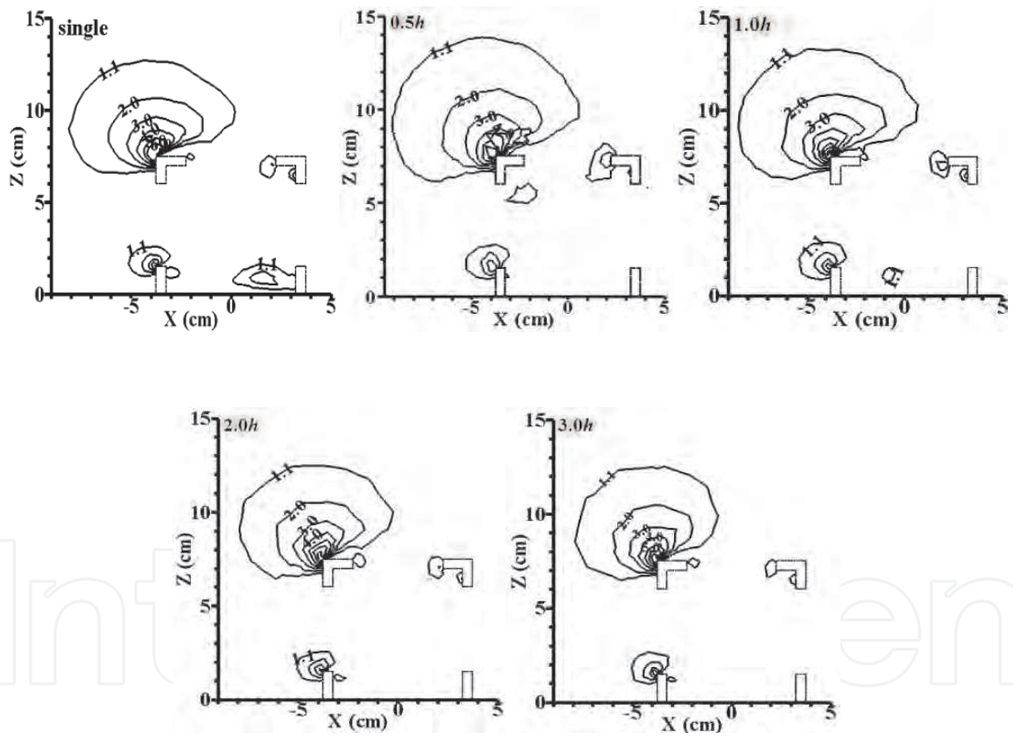

Fig. 17. Distribution of the upwelling field of a single and two parallel hollow cube artificial reefs with different spacings by simulation (the inlet velocity is 11.0 cm/s)

Fig. 18 shows a long and narrow slow flow field spread at the rear of a single artificial reef. Along the forward direction of the x-axis, the maximum horizontal flow velocity appears within the artificial reef, and after that, the flow velocity first decreases and then increases.

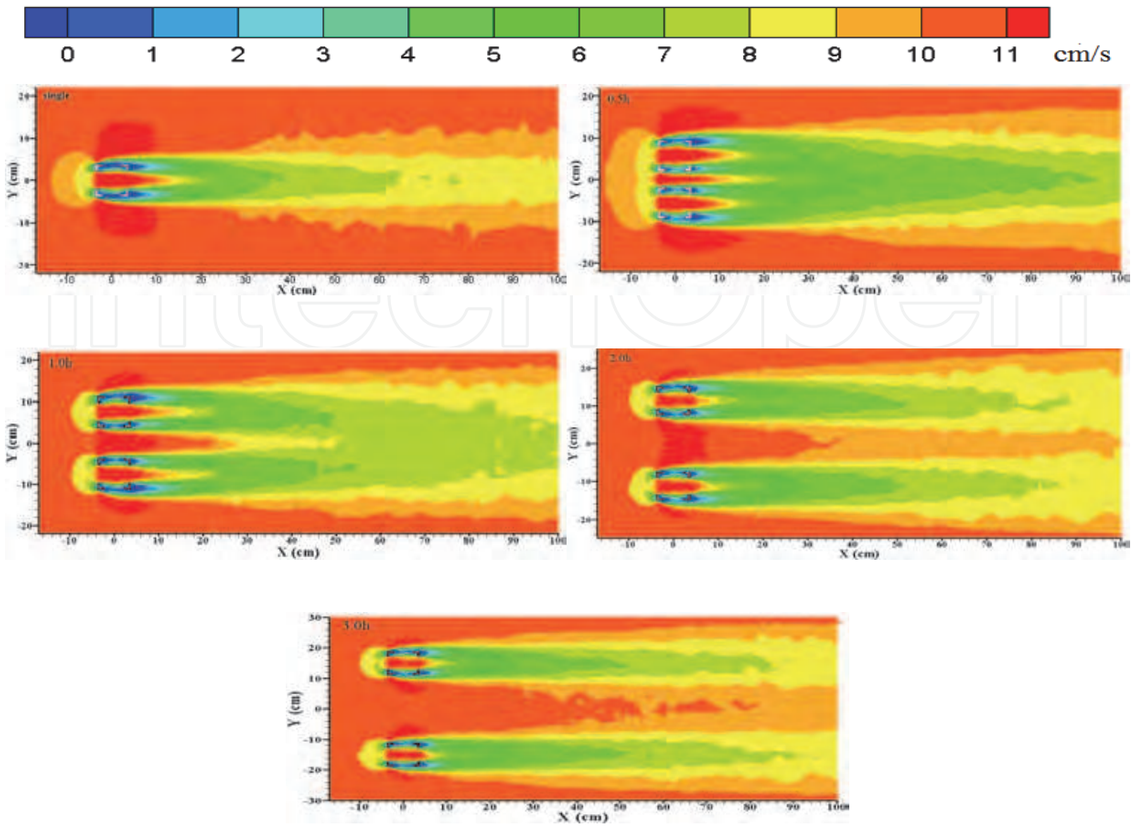

Fig. 18. Horizontal flow velocity contour plots of a single and two parallel artificial reefs with different spacings (the horizontal cross-section is $z=1/2h$, h=7.5 cm)

The mutual effect of two reefs is very strong, and the slow flow velocity fields in the front and the back of two artificial reefs nearly connect when the spacing is 0.5h. Thus, a larger area of slow velocity flow field is produced for a 0.5h gap distance. When the spacing increases to 1.0h, downstream of the reefs, the flow speed begins to increase, and the construction of the flow field presents a trend of separation. The slow velocity flow fields behind two artificial reefs are separated from each other by and large when the spacing is 2.0h. After that point, the structure of the flow field for each artificial reef becomes the same as the single condition, and the interaction between the two reefs is slight when the distance increases to 3.0h.

5.2 Two vertical hollow cube artificial reefs

Fig. 19 compares the upwelling field of two vertical artificial reefs with different spacings. As shown in the graphs, for different spacings, the latter artificial reef causes little impact on the upwelling field of the first artificial reef. With different spacings, the scales of the upwelling field of the first reef are the same as that of a single reef. Nevertheless, with the increase of the vertical spacing from 2.0h to 12.0h, the height of the upwelling field of the second incident flow artificial reef increases gradually. When the spacing is 12.0h, the height of the upwelling field of two artificial reefs is close, but the area gap is greater.

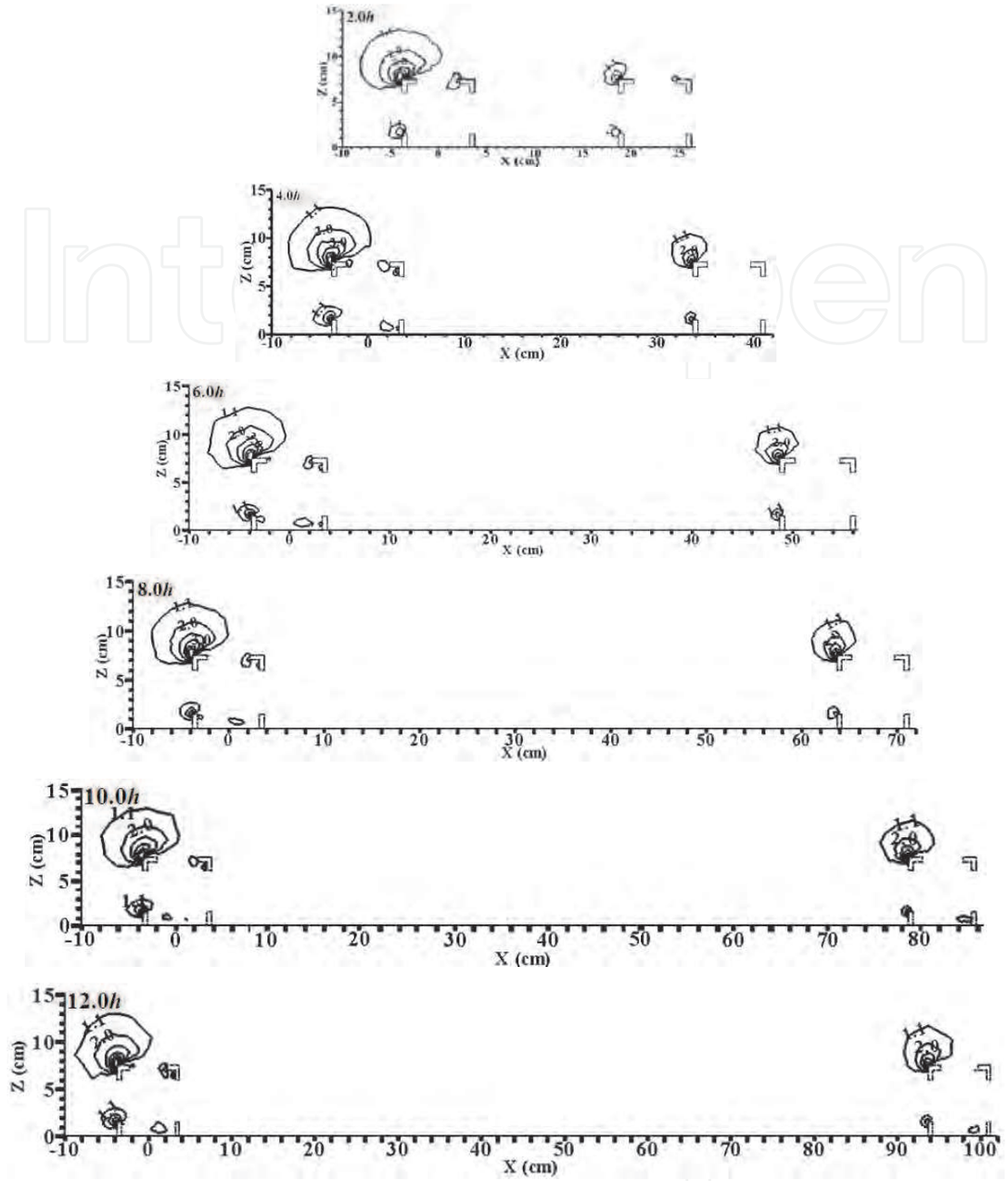

Fig. 19. Distribution of the upwelling field of a single and two vertical hollow cube artificial reefs with different spacings by simulation (the inlet velocity is 11.0 cm/s)

As shown in Fig. 20, the flow fields between two reefs are constantly changing with increasing spacing. The horizontal flow field structure of two artificial reefs with 1.0*h* spacing is similar to that of a single reef. With the spacing of two reefs added to 2.0h, the construction of the flow field presents a trend of separation. When the spacing is 4.0*h*, the flow velocity in most areas between the two reefs is slow after that the flow velocity increase gradually with the spacing. The interactions of two artificial reefs are first strengthened and then weakened with increasing distance.

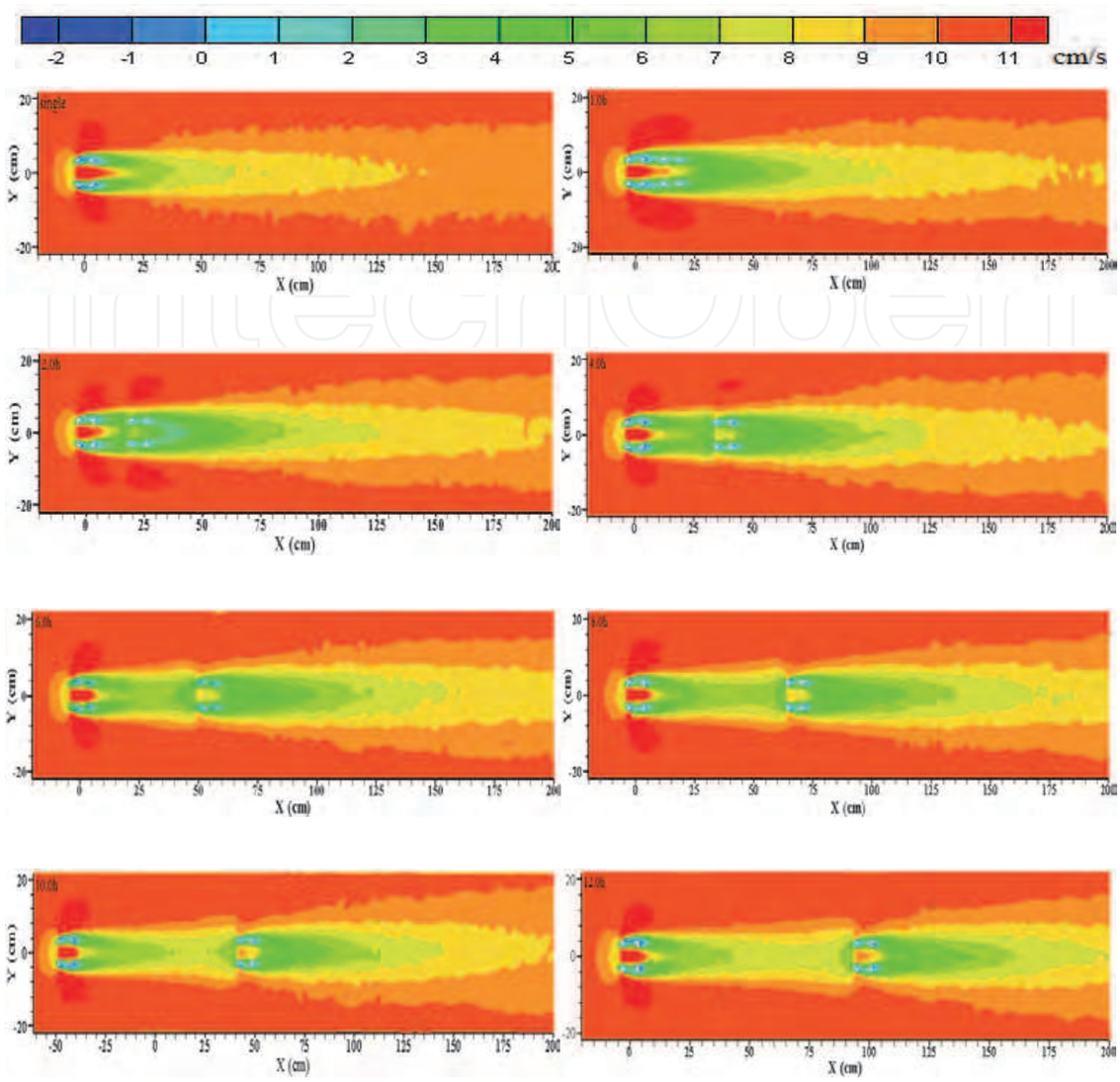

Fig. 20. Horizontal flow velocity contour plots of a single and two artificial reefs with different spacings (Z=0.5*h*)

Fig. 21 shows that the flow velocity within and in the front of the first artificial reef with different spacings is approximately equal to that of a single reef; however, the flow velocities in the rear of two reefs are less than that of the single condition. The same distribution regularity of the flow velocity between two artificial reefs is obtained for different spacings. The flow velocity decreases first and then increases suddenly in the front field of the second artificial reef. The same distribution rules for flow velocities also exist in the rear of the two reefs for different spacings. When the spacing is 4.0*h*, the minimum flow velocity in the area between the two artificial reefs has a minimum value; after that point, it increases with spacing. It was also found that the minimum velocity in the back of the two reefs is acquired at the spacing of 2.0*h*, and a large gap was found compared with other conditions. After the key point in the back field of two reefs where the flow velocity is the minimum, a larger spacing leads to a lower flow velocity.

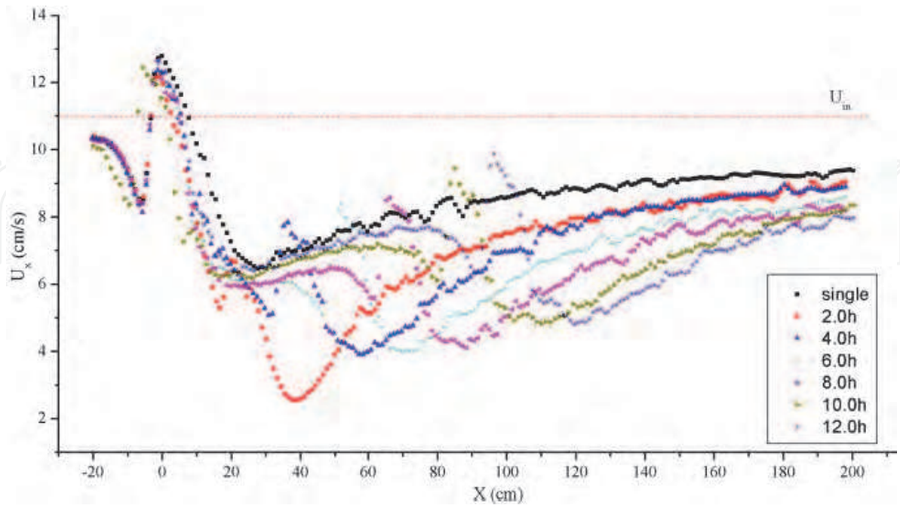

Fig. 21. Distribution of the horizontal flow velocities of two vertical artificial reefs along the line of Y=0 at the horizontal cross-section of Z=1/2*h* (*h*=7.5 cm)

6. Conclusions

Some main conclusions can be drawn as follows:

1. The flow field within and around a single hollow cube artificial reef was investigated by physical experiments and numerical simulations. The upwelling and back vortex flow fields that arose from artificial reefs were analyzed by using qualitative and quantitative analysis methods. According to the comparisons, there is a good agreement between the numerical and experimental results.
2. Based on the experimental verification, a detailed numerical study was conducted to investigate the effect of reef height on the structure of the flow field. The height and area of upwelling current region increased linearly and nonlinearly with increasing reef height, respectively. When the value of r (the reef height to water-depth) was 0.2, the normalized maximum and average upwelling flow velocities reached their maximum values. An exponential growth relationship existed between the length of the back vortex flow and the reef height. The flow field on either side of artificial reef was also discussed. A preferable unit artificial reef effect was achieved when the ratio of the reef height to water-depth was 0.2.
3. In the meantime, the influence of the arrangement (parallel and vertical) and spacing on the flow field of the two artificial reefs were discussed using the results of the numerical method. In the parallel combination, the scale of the upwelling field reached the maximum value, and a larger area of slow velocity flow field was obtained. The interaction between the two reefs was slight after the spacing became larger than 2.0*h*. In the vertical combination, the latter artificial reef had a weaker effect on the distribution of flow velocities within and in the front of the first artificial reef. When the

spacing was 4.0*h*, the flow velocity in the area between the two reefs obtained the minimum value. Behind the two reefs, the lowest flow velocity was achieved at a spacing of 2.0*h*, and, at a larger spacing, there was a lower flow velocity.

7. Acknowledgments

This work was financially supported by the National Natural Science Foundation (NSFC) Project No.50809014 and 50921001, the National 863 High Technology Project No.2006AA100301, the Specialized Research Fund for the Doctoral Program of Higher Education No.200801411094 and Special Fund for Agro-scientific Research in the Public Interest Project NO.201003068.

8. References

Baine, M. (2001). Ocean & Coastal Management. *Artificial reefs: a review of their design, application, management and performance*, Vol.44, No.3-4, pp. 241-259

Einbinder, S.; Perelberg, A. & Ben-Shaprut, O, et al. (2006). MARINE ENVIRONMENTAL RESEARCH. *Effects of artificial reefs on fish grazing in their vicinity: Evidence from algae presentation experiments,* Vol.61, No.1, pp. 110-119

Hixon, M.A. & Beets, J.P. (1989). BULLETIN OF MARINE SCIENCE. *SHELTER CHARACTERISTICS AND CARIBBEAN FISH ASSEMBLAGES: EXPERIMENTS WITH ARTIFICIAL REEFS,* Vol.44, No.2, pp. 666-680

Jensen, A. (June 1998). *European Artificial Reef Research Network (EARRN): Final Report and Recommendations*. Published by the University of Southampton.

Leitao, F.; Santos, MN. & Erzini, K, et al. (2008). MARINE BIOLOGY. *The effect of predation on artificial reef juvenile demersal fish species,* Vol.153, No.6, pp. 1233-1244

Lin, J. & Zhang, S.Y. (2006). Marine Fisheries. *Research advances on physical stability and ecological effects of artificial reef*. Vol.28, No.3, pp. 257-262

Liu, H.S.; Ma, X. & Zhang, S.Y., et al. (2009). *Validation and comparison between wind tunnel experiments and numerical simulation of flow field around artificial reefs* Vol.16, No.3, pp. 365-371

Pan, L.Z.; Lin, J. & Zhang, S.Y. (2005). Journal of Shanghai Fisheries University. *A numerical experiment of the effects of artificial reef on vertical2-dimensional steady flow field.* Vol.14, No.4, pp. 406-412

Seaman, W. (2007). Hydrobiologia. *Artificial habitats and the restoration of degraded marine ecosystems and fisheries*, Vol.580, No.1, pp. 143-155

Su, D.T.; Liu, T.L. & Ou, C.H. (2007). *A Comparison of the PIV Measurements and Numerical Predictions of the Flow Field Patterns within an Artificial Reef.* In: 17th international offshore and polar engineering conference, Lisbon, Vol. 1-4. pp. 2239-2245.

Walker, B.K.; Henderson, B. & Spieler, R.E. (April 2002). Aquatic Living Resources. *Fish assemblages associated with artificial reefs of concrete aggregates or quarry stone offshore Miami Beach, Florida, USA,* Vol.15, No.2, pp. 95-105

Williams, T.W. (August 2006). *Sinking Poor Decision Making With Best Practices: A Case Study of Artificial Reef Decision-Making in the Florida Keys,* Virginia Commonwealth University, America.

Zhang, H.H. & Sun L. (2001). Resources Science. *On reproduction increase of the sea aquatic resources by artificial fish-reef engineering*. Vol.23, No.5, pp. 6-10

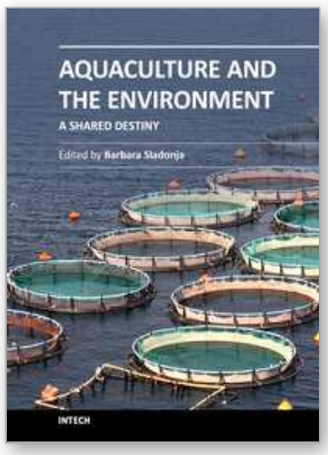

Aquaculture and the Environment - A Shared Destiny

Edited by Dr. Barbara Sladonja

ISBN 978-953-307-749-9
Hard cover, 246 pages
Publisher InTech
Published online 22, December, 2011
Published in print edition December, 2011

Aquaculture is the art, science and business of cultivating aquatic animals and plants in fresh or marine waters. It is the extension of fishing, resulted from the fact that harvests of wild sources of fish and other aquatic species cannot keep up with the increased demand of a growing human population. Expansion of aquaculture can result with less care for the environment. The first pre-requisite to sustainable aquaculture is clean wate, but bad management of aquatic species production can alter or even destroy existing wild habitat, increase local pollution levels or negatively impact local species. Aquatic managers are aware of this and together with scientists are looking for modern and more effective solutions to many issues regarding fish farming. This book presents recent research results on the interaction between aquaculture and environment, and includes several case studies all over the world with the aim of improving and performing sustainable aquaculture.

InTech Europe
University Campus STeP Ri
Slavka Krautzeka 83/A
51000 Rijeka, Croatia
Phone: +385 (51) 770 447
Fax: +385 (51) 686 166
www.intechopen.com

InTech China
Unit 405, Office Block, Hotel Equatorial Shanghai
No.65, Yan An Road (West), Shanghai, 200040, China
中国上海市延安西路65号上海国际贵都大饭店办公楼405单元
Phone: +86-21-62489820
Fax: +86-21-62489821

IntechOpen